AIAA SciTech
4-8 January 2016, San Diego, California, USA
54th AIAA Aerospace Sciences Meeting

Krypton Tagging Velocimetry (KTV) in Supersonic Turbulent Boundary Layers

D. Zahradka* N. J. Parziale†
Stevens Institute of Technology, Hoboken, NJ 07030, USA
M. S. Smith‡ E. C. Marineau§
AEDC White Oak, Silver Spring, MD 20903, USA

The krypton tagging velocimetry (KTV) technique is applied to the turbulent boundary layer on the wall of the Mach 3 Calibration Tunnel at Arnold Engineering Development Complex (AEDC) White Oak. Profiles of velocity were measured with KTV and Pitot-pressure probes in the Mach 2.75 turbulent boundary layer comprised of 99% N_2/1% Kr at momentum-thickness Reynolds numbers of $Re_\Theta = 800$, 1400, and 2400. Agreement between the KTV- and Pitot-derived velocity profiles is excellent. The KTV and Pitot velocity data follow the law of the wall in the logarithmic region with application of the Van Driest I transformation. Also, the velocity data in the wake region are consistent with data from the literature for a turbulent boundary layer with a favorable pressure gradient history. A modification of the Mach 3 AEDC Calibration Tunnel is described which facilitates operation at several discrete unit Reynolds numbers consistent with AEDC Hypervelocity Tunnel 9 run conditions of interest. Moreover, to enable near-wall measurement with KTV, an 800 nm longpass filter was used to block the reflection and scatter from the 760.2 nm read-laser pulse. With the longpass filter, the 819.0 nm emission from the re-excited Kr can be imaged to track the displacement of the metastable tracer without imaging the reflection and scatter from the read laser off of solid surfaces.

Nomenclature

$\dot{m}$	Mass-flow-rate, (kg/s)
C	Discharge Coefficient, (-)
A	Area, (m^2)
γ	Ratio of specific heats, (-)
ρ	Density, (kg/m^3)
P	Pressure, (Pa)
t	Time, (s)
τ	Timescale, (1/s)
k_q	Quenching Rate Constant, (cm^3/(molecule s))
Ru	Universal Gas Constant ((Pa m^3)/(kg mol K))
T	Temperature, (K)
M	Mach Number, (-)
Re	Reynolds Number, (-)
U	Velocity, (m/s)
u_τ	Friction velocity, (m/s)
x	Distance, (m)
r	Recovery Factor, (-)

*Graduate Student, Mechanical Engineering, Castle Point on Hudson, Hoboken, New Jersey, 07030.
†Assistant Professor, Mechanical Engineering, Castle Point on Hudson, Hoboken, New Jersey, 07030, AIAA Member.
‡Senior Research Engineer, Aerospace Testing Alliance, Silver Spring, MD 20903, Senior AIAA Member.
§Lead Aerospace Technologist, AEDC White Oak, Silver Spring, MD 20903, AIAA Member.

Δx Displacement Distance, (m)
Δt Change in Time, (s)
Θ Momentum Thickness
Δ^* Integral Length Scale for Momentum Thickness, (m)
c Sound speed, (m/s)

Subscript
OP Orifice Plate
A Ambient
noz Nozzle
R Reservoir
m Metastable
∞ Free Stream
Θ Based on Momentum Thickness
02 Pitot
w Wall
e Edge
r Recovery

I. Introduction

The need to accurately assess the heat transfer, skin friction, and velocity profiles on high-speed vehicles is born out of a thrust for rapid space access[1] and conventional prompt global strike (CPGS).[2] Progress has been made in the computation of high-speed and reacting flows, as reviewed in Candler[3] and Schwartzentruber and Boyd.[4] Moreover, the uncertainty that arises from the application of the state-of-the-art (SOA) research codes to hypersonic problems has been characterized, as in Bose et al.[5] Obtaining test and evaluation (T&E) data for high-speed vehicle development[6]and validation data for SOA research codes is the motivation for the development of new experimental diagnostics, especially in demanding testing environments.

There are a number of methodologies for making velocity measurements in fluid flows such as pressure-based measurement, thermal anemometry, and particle based techniques (laser-Doppler velocimetry, global-Doppler velocimetry, and particle image velocimetry (PIV)).[7] The measurement of velocity with pressure-based and thermal anemometry methods are refined in that they can consistently yield data with low uncertainty; however, these techniques are intrusive, which eliminates them as candidates in certain flow regimes. Moreover, frequency response, spatial resolution, and required assumptions regarding the local temperature are limitations for velocity measurement using Pitot probes. Particle-based methods of velocimetry, PIV in particular, can currently produce multi-component velocity data. And after post-processing, PIV can yield field information about vorticity and pressure.

An alternative velocimetry technique, tagging velocimetry,[8] will be the focus of this paper. Tagging velocimetry is typically performed in gases by tracking the fluorescence of a native, seeded, or synthesized gas. In contrast to the limitations of implementing PIV techniques in high-speed facilities, the implementation of tagging velocimetry is not limited by timing issues associated with tracer injection[9] or reduced particle response at Knudsen and Reynolds numbers[10] typical of high-speed windtunnels. Noted methods of tagging velocimetry include the VENOM,[11–15] APART,[16–18] RELIEF,[19–23] FLEET,[24,25] iodine,[26,27] acetone,[28–30] and the hydroxyl group[31–33] techniques among others.[34–37]

In this paper, we first present the KTV setup and excitation/emission scheme with the longpass filter in place. We present KTV results with the new excitation/emission scheme as applied to an underexpanded jet to assess the SNR. We then describe a modification of the Mach 3 AEDC Calibration Tunnel which facilitates operation at several discrete unit Reynolds numbers consistent with AEDC Hypervelocity Tunnel 9 run conditions of interest. We present KTV and Pitot-probe based velocity measurements for a Mach 2.75 turbulent boundary layer. Finally, we non-dimensionalize the velocimetry results, first with application of the Van Driest I transformation, and lastly with a scaling of the data in the wake region.

II. Krypton Tagging Velocimetry (KTV) Setup

Krypton Tagging Velocimetry (KTV),[38,39] relative to other tagging velocimetry techniques, relies on a chemically inert tracer. This property may enable KTV to broaden the utility of tagging velocimetry because the technique can be applied in gas flows where the chemical composition is difficult to prescribe or predict. The use of a metastable noble gas as a tagging velocimetry tracer was first suggested by Mills et al.[40] and Balla and Everhart.[41] KTV was first demonstrated by Parziale et al.[38,39] to measure the velocity along the center-line of an underexpanded jet of N_2/Kr mixtures. In that work, pulsed tunable lasers were used to excite and/or induce fluorescence of Kr atoms that were seeded into the flow for the purposes of position tracking.

The excitation/emission scheme used in this work is slightly different than in the original work by Parziale et al.[38,39] A high-precision 800 nm longpass filter (Thorlabs FELH0800) is used to block the read-laser beam with the intent of minimizing the noise resulting from the read-laser pulse reflection and scatter from solid surfaces. This was done to enable the imaging of fluorescing Kr atoms near the windtunnel wall.

Following the energy level diagram in Fig. 1, KTV is performed as follows:
1) Seed a base flow with krypton locally or globally.
2) Photosynthesize metastable krypton atoms with a pulsed tunable laser to form the tagged tracer: two-photon excitation of $4p^6(^1S_0) \rightarrow 5p[3/2]_2$ (214.7 nm) and rapid decay to metastable states $5p[3/2]_2 \rightarrow 5s[3/2]_1^o$ (819.0 nm) and $5p[3/2]_2 \rightarrow 5s[3/2]_2^o$ (760.2 nm).
3) Record the displacement of the tagged metastable krypton by imaging the laser induced fluorescence (LIF) that is produced with an additional pulsed tunable laser: re-excite $5p[3/2]_2$ level by $5s[3/2]_2^o \rightarrow 5p[3/2]_2$ transition with laser sheet (760.2 nm) and read spontaneous emission of $5p[3/2]_2 \rightarrow 5s[3/2]_1^o$ (819.0 nm) transitions with a camera positioned normal to the flow.

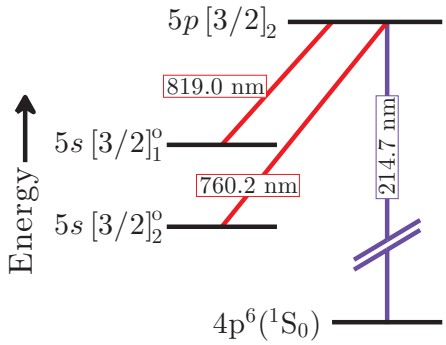

Figure 1. Energy level diagram for KTV.

The experiment was run using two tunable lasers to provide the 214.7 nm (write) and 760.2 nm (read) laser beams required for KTV (schematic in Fig. 2). The write laser consisted of a frequency tripled PR8010 Nd:YAG laser and a frequency doubled Continuum ND6000 Dye Laser. The Nd:YAG laser pumped the dye laser with 400 mJ/pulse at a wavelength of 355 nm. The dye in the laser was Coumarin 440 and the laser was tuned to output a 429.4 nm beam. Frequency doubling of the dye laser output was preformed using an Inrad BBO-C (65°) crystal placed in a Inrad 820-360 gimbal mount, resulting in a laser beam with two wavelengths, 214.7 nm and 429.4 nm. The 214.7 nm and 429.4 nm beams were separated with a Pellin-Broca prism. The 429.4 nm wavelength beam was sent to a beam dump and the 214.7 nm wavelength beam was directed to the test section. The read laser consisted of a frequency doubled Continuum NY82S-10 Nd:YAG laser and a Continuum ND60 Dye Laser. The Nd:YAG laser pumped the dye laser with 250 mJ/pulse at a wavelength of 532 nm. The dye in the laser was LDS 765 and the laser was tuned to output a 760.15 nm beam.

The write-laser beam setup resulted in approximately 1 mJ/pulse, with a wavelength of 214.7 nm, a linewidth of approximately 10 cm^{-1}, a pulsewidth of approximately 7 ns, and a repetition rate of 10 Hz. The write-laser beam was directed into the test section with 1 inch 5th-harmonic Nd:YAG laser mirrors (IDEX Y5-1025-45) and focused to a narrow waist into the test section with a 1000 mm fused silica lens. Assuming Gaussian beam propagation, the waist diameter was $\approx$ 55 µm, the peak beam fluence was $\approx$ 21 J/cm^2, and the

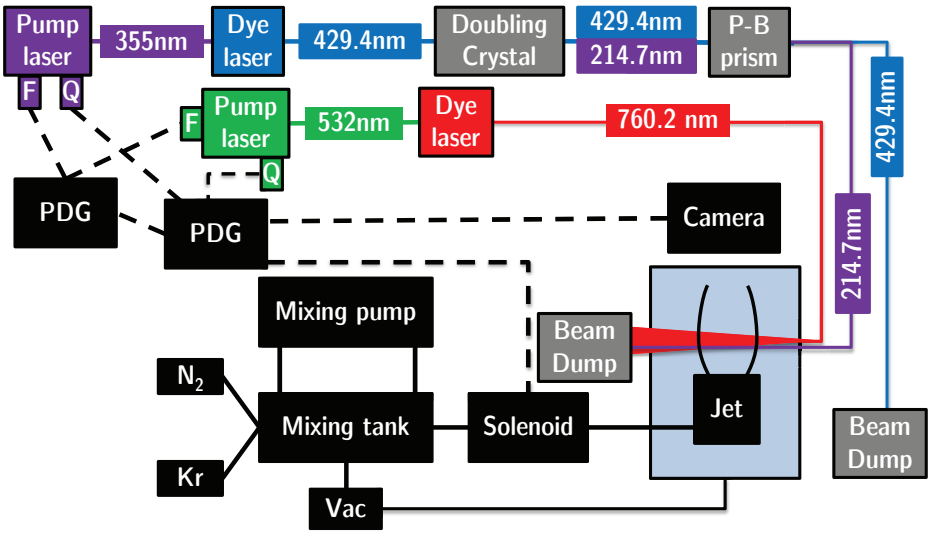

Figure 2. Setup of bench test experiment with lasers, test section, and appropriate wavelengths of laser beams.

Rayleigh length was ≈ 44 mm. This narrow laser beam photosynthesizes the metastable krypton atoms that comprise the tracer forming the "write line."

The read-laser beam setup resulted in approximately 20 mJ/pulse, with a wavelength of 760.15 nm, a linewidth of approximately 10 cm^{-1}, a pulsewidth of approximately 8 ns, and a repetition rate of 10 Hz. The read-laser beam was directed into the test section using 2 inch broadband dielectric mirrors (Thorlabs BB2-E02) as a sheet of ≈ 200 µm thickness. This "read sheet" re-excites the metastable Kr tracer atoms so that their displacement can be measured.

The read sheet must overlap the write line at the anticipated position after the delay between the write and read laser pulses. Example burn patterns that illustrate the beam locations prior to performing an experiment are presented as Fig. 3(a). In Fig. 3(b), the "hot" portion of the laser beams are identified with a narrow, red ellipse indicating the approximate spatial bound of the read sheet and a violet circle indicating the same of the write line. Note that these are not indicative of beam size because the burn patterns are produced after approximately 10 pulses from the write and read lasers, which tend to overexpose the burn paper.

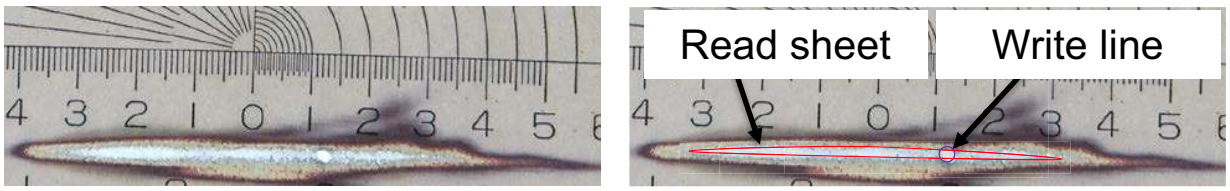

(a) (b)

Figure 3. Burn pattern overlaps of the write and read lasers. Size is illustrated in (a) and the "hot" portion of the beams are annotated in (b). The ruler in the background is in millimeters.

The laser and camera timing is controlled by pulse/delay generators. The flash lamps and the Q-switches of the Nd:YAG lasers are triggered to cycle at 10 Hz by one pulse/delay generator (SRS DG535). Another pulse/delay generator (SRS DG535) is used to control camera timing and gate width. For the underexpanded jet experiments, an additional BNC 505-4C pulse/delay generator is set to single-shot mode to trigger the solenoid to the jet.

The intensified camera used for all experiments is a 16-bit Princeton Instruments PIMAX-2 1024x1024 with an 18 mm Gen III Extended Blue intensifier. The gain is set to 255 with 2x2 pixel binning to ensure a 10 Hz frame rate. The camera gate was opened for 50 ns to bracket the read-laser pulse so as to capture the spontaneous emission of $5p[3/2]_2 \rightarrow 5s[3/2]_1^o$ (819.0 nm) transitions.

III. Underexpanded Jet

In this section, we present the setup and results of an underexpanded jet comprised of a 99% N_2 / 1% Kr mixture. The purpose of this series of experiments was to recreate the results in Parziale et al.[38,39] while assessing the SNR with the modified excitation/emission scheme that utilizes a 800 nm longpass filter. In Parziale et al.,[38,39] the 760.2 nm and 819.0 nm transitions were imaged after re-excitation. With two 800 nm longpass filters in series in front of the image intensifier, signal from the 760.2 nm transition is lost; however, the noise resulting from the scatter and reflection of the read laser at 760.2 nm is reduced, as well. At 760.2 nm, the manufacturer reports a transmission of 5e-4% for one 800 nm longpass filter.

The metastable krypton tracer is written approximately two diameters from the jet orifice. A series of 6 exposures is presented as Fig. 4. In this series, the camera gate is chosen to bracket only the spontaneous emission of $5p[3/2]_2 \rightarrow 5s[3/2]_1^o$ (819.0 nm) transitions. The modified scheme reproduces the results from Parziale et al.,[38,39] but with two high-precision 800 nm longpass filter in series place to block the noise resulting from the reflection and scatter of the 760.2 nm read sheet from solid surfaces. Ultimately, the signal-to-noise ratio (SNR) in Fig. 4 was sufficient to justify using this excitation/emission strategy in the Mach 3 AEDC Calibration Tunnel.

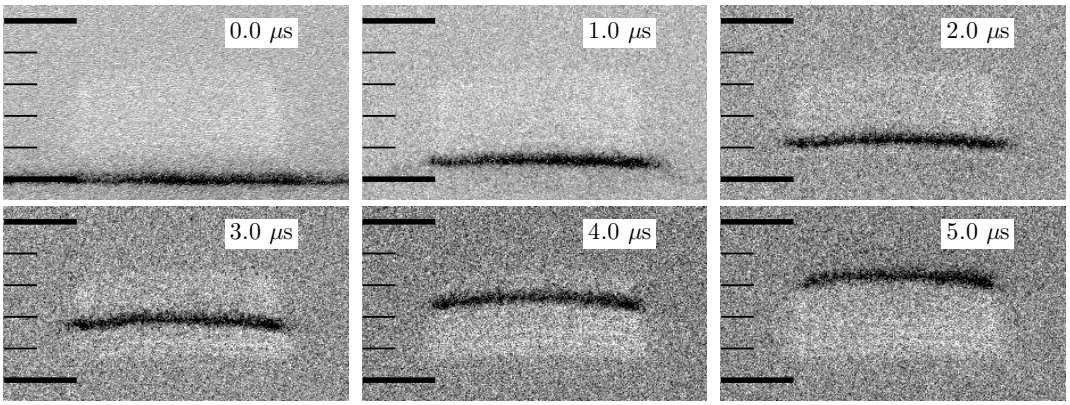

Figure 4. KTV in a 99% N_2 / 1% Kr underexpanded jet. Inverted intensity scale. The camera gate is fixed to include only the read laser pulses (after the first image). The time stamp of the delay between the write and read pulses is given in μs. Major tick marks at 5 mm intervals.

IV. Mach 3 AEDC Calibration Tunnel and Modification

The purpose of conducting KTV experiments in the Mach 3 AEDC Calibration Tunnel was to demonstrate that the technique could be utilized in AEDC Hypervelocity Tunnel 9,[42,43] which is a large-scale N_2 blow-down hypersonic windtunnel. The Mach 3 AEDC Calibration Tunnel is a large vacuum tank with a converging-diverging nozzle attached to it. To start the tunnel, a valve is cycled downstream of the nozzle throat. The effective reservoir is the ambient laboratory air and so the freestream conditions are fixed.

The Mach 3 AEDC Calibration Tunnel and AEDC Tunnel 9 operate with different run conditions; that is, AEDC Tunnel 9 typically operates with a lower freestream pressure than does the Mach 3 AEDC Calibration Tunnel. This has implications on the SNR of the KTV technique because of the population available for fluorescence[44] and the quenching of the metastable Kr tracer.

To account for the difference in pressure, modifications were made to the tunnel upstream of the nozzle (boxed in red in Fig. 5). The effective reservoir pressure was reduced by choking the flow upstream of the throat with an orifice plate. A PVC pipe housed perforated screens that were used to breakup the jet from the orifice plate which was a PVC end cap with a hole drilled in it. Three caps with holes of diameter 12.7 mm, 19.1 mm, and 25.4 mm were used to alter the mass-flow rate, and thus effective pressure drop.

To estimate the reduced reservoir pressure, choked flow calculations[45] were used where sonic flow was assumed at the orifice plate and nozzle throat. The mass-flow-rate of the gas into the tube from the ambient lab to

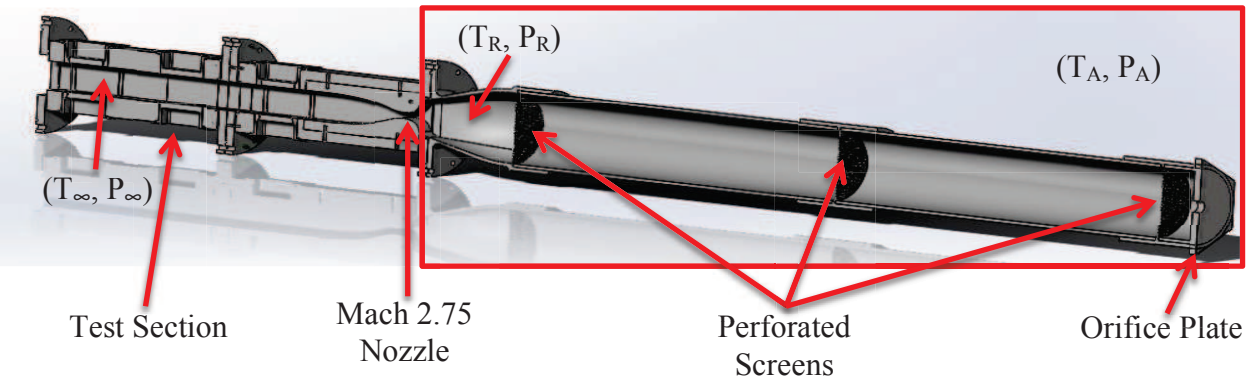

Figure 5. Modification and test section of Mach 3 AEDC Calibration Tunnel. The modification is boxed in red.

the effective reservoir was determined using

$$\dot{m} = C_{\mathrm{OP}} A_{\mathrm{OP}} \sqrt{\gamma \rho_A P_A \left(\frac{2}{\gamma+1}\right)^{\frac{\gamma+1}{\gamma-1}}} \tag{1}$$

and then the mass-flow-rate of the gas into the tube from effective reservoir to the freestream was determined using

$$\dot{m} = C_{\mathrm{noz}} A_{\mathrm{noz}} \sqrt{\gamma \rho_R P_R \left(\frac{2}{\gamma+1}\right)^{\frac{\gamma+1}{\gamma-1}}} \tag{2}$$

where the subscripts "OP" and "noz" refer to the orifice plate and the nozzle, respectively. We assume that the flow is steady so that the mass-flow-rates in Eqs. 1 and 2 must match. Furthermore, we assume that the discharge coefficients, C_{OP} and C_{noz} are unity and that there are no standing shock waves wihtin the tube (no change in total pressure). Equating Eqs. 1, and 2 and solving for P_R results in

$$P_R = P_A \sqrt{\frac{T_R}{T_A}} \frac{A_{\mathrm{OP}}}{A_{\mathrm{noz}}}. \tag{3}$$

Assuming that the expansion through the orifice plate and perforated screens (refer to Fig. 5) is isothermal, we find that the effective reservoir pressure could be reduced by a factor of approximately 2, 4, and 10 for the 25.4 mm, 19.1 mm, and 12.7 mm orifice plates, respectively. Predicted freestream static pressure values for the 25.4 mm, 19.1 mm, and 12.7 mm orifice plates are 1920 Pa, 1080 Pa, and 480 Pa, respectively; these predicted static pressures are within 10% of the measured static pressures in Table 1. Ultimately, we are interested in the effect of orifice plate diameter on the freestream unit Reynolds number, and the predicted

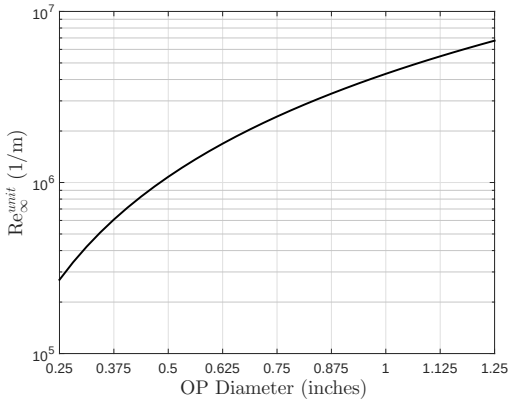

Figure 6. Predicted freestream unit Reynolds vs. orifice plate diameter.

unit Reynolds number is presented as Fig. 6. These calculations yield a promising strategy for controlling the Reynolds number of the flow in the Mach 3 AEDC Calibration Tunnel.

An isolation bag was added to the end of the tube over the orifice plate which isolates the test gas from the ambient air in the laboratory. The bag is flexible, so the test gas in the isolation bag is at constant ambient pressure throughout an experiment. The test section, PVC tube, and isolation bag could be filled with high-purity mixtures of nitrogen and krypton. The Mach 3 AEDC Calibration Tunnel experiment, with the modification, is shown in Fig. 7.

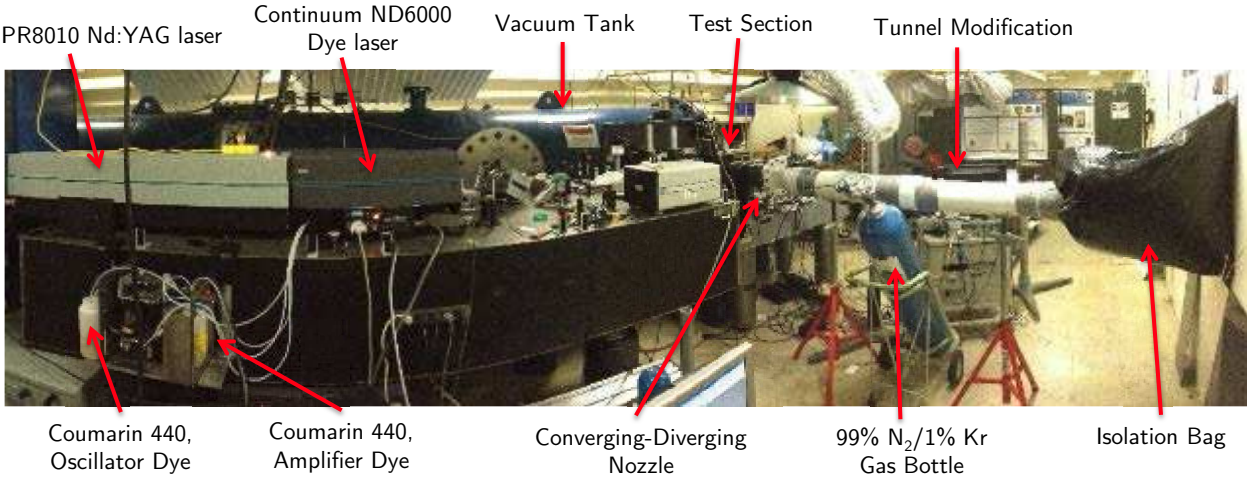

Figure 7. Mach 3 AEDC Calibration Tunnel experiment setup with annotations. Components not shown: NY82S-10Nd:YAG laser, Continuum ND60 Dye Laser and LDS 765 Amplifier and Oscillator Dye. The two lasers are located behind the write laser setup and the dye is located on the other side of the optical table.

The run conditions with each of the orifice plates were calculated by measuring the static and Pitot pressure with Micro Switch 130PC pressure transducers, and finding the freestream Mach number with the Rayleigh-Pitot probe formula[46]

$$\frac{P_{02}}{P_\infty} = \left(\frac{(\gamma+1)^2 M_\infty^2}{4\gamma M_\infty^2 - 2(\gamma-1)}\right)^{\left(\frac{\gamma}{\gamma-1}\right)} \left(\frac{1-\gamma+2\gamma M_\infty^2}{\gamma+1}\right). \tag{4}$$

The freestream temperature (and thus freestream velocity) were found by assuming isentropic expansion[46] as

$$T_\infty = T_R \left(1 + \frac{\gamma-1}{2} M_\infty^2\right)^{-1}. \tag{5}$$

It was determined that the expansion through the orifice plates and perforated screens was isothermal by thermocouple measurement of the reservoir temperature using an Omega 5TC-TT-E-40-36 thermocouple; that is, $T_R = T_A$. Freestream conditions for each orifice plate are listed in Table 1. Example measurements for the static pressure, Pitot pressure, and reservoir temperature are presented in Fig. 8(a); the freestream Mach number is presented as Fig. 8(b). The expansion wave that propagates through the PVC tube during tunnel startup can be seen between 0.75-2.0 seconds. The steady test time is approximately 3 seconds (between 2 and 5 seconds).

V. Effect of Run Condition on Metastable Lifetime

The SNR of a fluorescence technique is proportional to the local number density of the fluorescing constituent.[44] However, in the case of KTV, increasing the local number density also increases the decay rate of the photosynthesized metastable Kr $5s[3/2]_2^o$ tracer. This presents the researcher with the task of maximizing the SNR by balancing the local number density with the decay rate of the tracer. In this section, we present estimates of the relevant figures pertaining to the de-excitation rate of the metastable Kr tracer for flows of interest.

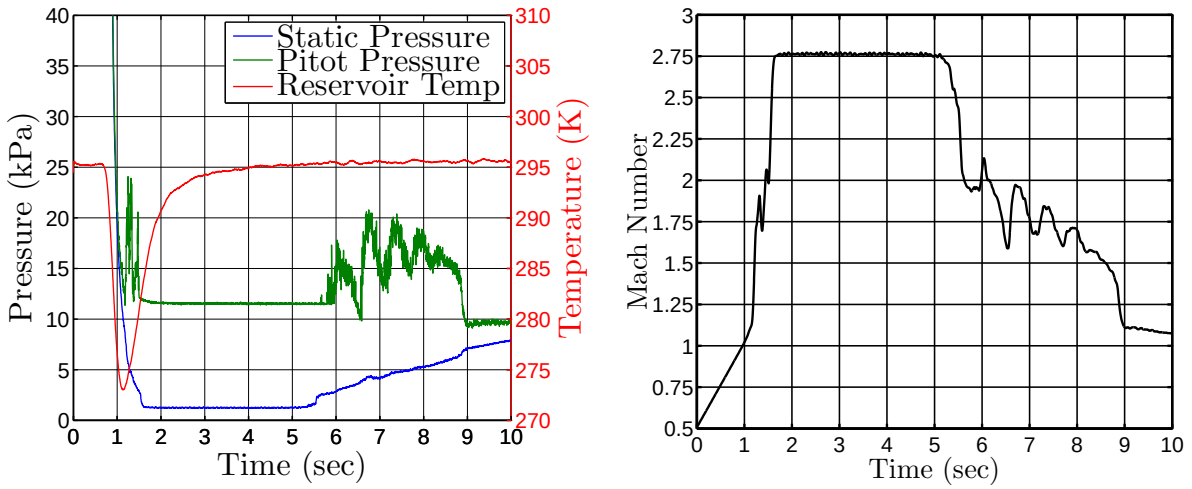

(a) (b)

Figure 8. Sample run conditions for the Mach 3 AEDC Calibration Tunnel for the 19.1 mm orifice plate. In (a), measurements of the static pressure, Pitot pressure, and reservoir temperature, used for the calculation of Mach number (b), and freestream velocity. The steady test time is observed to occur between approximately 2 and 5 seconds.

Table 1. Conditions for the estimation of the distance between the write and read locations for KTV in various experiments. M_∞, P_∞, T_∞, ρ_∞, $\mathrm{Re}_\infty^{unit}$, Re_Θ, and U_∞ are the Mach number, pressure, temperature, density, unit Reynolds number, momentum thickness Reynolds number, and velocity scale for each experiment. τ_m and x_m are the calculated time and distance scale for the decay of the metastable Kr state.

Experiment	M_∞ (-)	P_∞ (Pa)	T_∞ (K)	ρ_∞ (kg/m^3)	$\mathrm{Re}_\infty^{unit}$ (1/m)	Re_Θ (-)	U_∞ (mm/µs)	τ_m (µs)	x_m (mm)
Underexpanded Jet	5.00	340	49.3	0.024	79.7e6	-	0.714	4.5	3.2
Mach 3 AEDC Calibration Tunnel - 12.7 mm OP	2.75	550	118	0.016	1.26e6	800	0.614	7.6	4.7
Mach 3 AEDC Calibration Tunnel - 19.1 mm OP	2.77	1010	118	0.030	2.30e6	1400	0.612	4.1	2.5
Mach 3 AEDC Calibration Tunnel - 25.4 mm OP	2.73	1825	118	0.053	4.16e6	2400	0.611	2.1	1.4
AEDC Tunnel 9 Run 3742	9.86	600	53.4	0.038	15.0e6	-	1.469	3.15	4.6
Caltech T5 Shot 2773	5.93	6000	1014	0.020	1.80e6	-	3.860	5.98	23

Researchers have studied the quenching rates of the $5s[3/2]_2^o$ state with a number of collisional partners.[47–50] In the work of Velazco et al.,[48] they tabulate the quenching rate constants of the $5s[3/2]_2^o$ state with constituents of interest in the aerothermodynamics and combustion communities. Using the plug flow approximation, they used a flow reactor to determine the timescale of metastable state decay as

$$\frac{1}{\tau_m} = \frac{D_0}{\Lambda^2 P} + k_1 P + k_2 P + k_Q[Q], \tag{6}$$

where the first three terms are due to diffusion, and two-body and three-body de-excitation processes in the argon carrier gas, respectively. The fourth term, $k_Q[Q]$ is the timescale associated with the de-excitation of the metastable state with an added reagent; this is the rate which will dominate the de-excitation of metastable Kr atoms in typical fluid mechanics applications of interest to the aerothermodynamics community.

If we assume a fluorescence signal towards the high side of the 16-bit camera's dynamic range at the write location (which has been demonstrated with the current experimental setup), then the number of recordable metastable lifetimes is estimated as $2^{16} \approx \exp(-t/\tau_m)$. We take $\ln(2^{16}) \approx 10 = t/\tau_m$ which leads to the estimation that we can record the displacement of metastable Kr for approximately 10 lifetimes.

In Table 1, we list the relevant parameters for KTV measurement; namely, local density, ρ_∞, and the length scale, x_m. The length scale, x_m, is computed as the product of the timescale from Eq. 6, the local velocity scale, U_∞, and a factor of 10 to account for the 10 metastable lifetimes that are recorded as $x_m = 10\tau_m U_\infty$.

We note that in Table 1, the estimated lifetime of the metastable tracer is approximately the same for the

Mach 3 AEDC Calibration Tunnel and AEDC Tunnel 9. This means that experiments in the Mach 3 AEDC Calibration Tunnel are a good simulation of future Tunnel 9 experiments. For-longer term goals, we plan to use KTV to measure the velocity profiles over flight-vehicle models in AEDC Tunnel 9 and high-enthalpy impulse facilities like Caltech's T5 reflected shock tunnel.[51] The useful length scale for each of these facilities was derived from Marineau et al.[52] (Tunnel 9) and Parziale et al.[39] (T5). In Table 1, it is seen that the metastable lifetime (τ_m) and the displacement distance (x_m) to be are estimated to be sufficient as to permit KTV measurements in Tunnel 9 or T5.

VI. Krypton Gas Bottle Cost

Krypton gas-bottle cost is appropriate for laboratory-scale KTV efforts. In this work, we performed approximately ≈100 experiments with approximately ≈4k USD worth of pre-mixed research grade krypton, yielding a ≈40 USD per experiment cost. We initially estimated that the seeding cost per run of 1% Kr mole fraction ranges from ≈10 USD in impulse facilities (e.g, Ludwieg Tubes, shocktunnels, and moderate reservoir pressure blow-down facilities) to ≈50-500 USD in high reservoir pressure long-duration blow-down hypersonic tunnels (e.g., Tunnel 9 at AEDC White Oak[43]). The range of cost is dependent on the unit Reynolds number (through local number density) the facility is to be run operated at; for the Tunnel 9 condition listed in Table 1 ($\mathrm{Re}_\infty^{unit}$ = 15e6 1/m), the estimated cost is ≈200 USD which is a small fraction of large-scale tunnel operation costs.

VII. Supersonic Turbulent Boundary Layer Results

In this section, we present KTV and Pitot-derived velocity profiles of the turbulent boundary layer on the wall of the AEDC White Oak Mach 3 Calibration Tunnel. The freestream was comprised of 99% N_2/1% Kr at momentum-thickness Reynolds numbers of $\mathrm{Re}_\Theta = \rho_e U_e \Theta/\mu_e$ = 800, 1400, and 2400. The momentum thickness is defined as

$$\Theta = \int_0^\infty \frac{\rho}{\rho_e}\frac{U}{U_e}\left(1-\frac{U}{U_e}\right)dy. \tag{7}$$

Pitot-derived velocity profiles were made at discrete wall-normal distances with Pitot and static pressure measurement using the same methodology as Brooks et al.[53,54] The Mach number was found with the Rayleigh-Pitot probe formula (Eq. 4).[46] The local temperature was found using Walz's[55] relation

$$\frac{T}{T_e} = \frac{T_w}{T_e} + \frac{T_r - T_w}{T_e}\left(\frac{U}{U_e}\right) - r\frac{\gamma-1}{2}M_e^2\left(\frac{U}{U_e}\right)^2 \tag{8}$$

with the recovery temperature T_r is defined as

$$\frac{T_r}{T_e} = 1 + r\frac{\gamma-1}{2}M_e^2. \tag{9}$$

KTV measurements were performed by tracking the tagged Kr center-of-mass locations for a prescribed time. Example exposures that illustrate the unsteady nature of the supersonic turbulent boundary layer are presented as Fig. 9. Each exposure is processed with a 3 pixel x 3 pixel (≈ 291 µm x 291 µm) two-dimensional Wiener adaptive-noise removal filter in MATLAB. Then, a Gaussian model of the form $f(x) = a\exp\left(-((x-b)/c)^2\right)$ is fitted to the intensity vector for each exposure in the x-direction for each row of pixels in the wall-normal direction (≈ 97 µm wall-normal direction x 5.0 mm streamwise direction). The centroid (b) and the 95% confidence bounds are determined with the non-linear least squares method. The streamwise displacement distance, Δx, is then found as the read-centroid location relative to the write-centroid location. The local velocity is found as $U = \Delta x/\Delta t$, where Δt is prescribed by a pulse/delay generator as Δt = 2 µs.

We present the dimensional velocity profiles for three conditions with Re_Θ=800 (Fig. 10(a)), Re_Θ=1400 (Fig. 10(b)), and Re_Θ=2400 (Fig. 10(c)). The KTV results are reported along with Pitot-tube derived velocity measurements and predicted turbulent profiles from the Virginia Tech (VT) Compressible Turbulent Boundary Layer applet from Devenport and Schetz.[56,57]

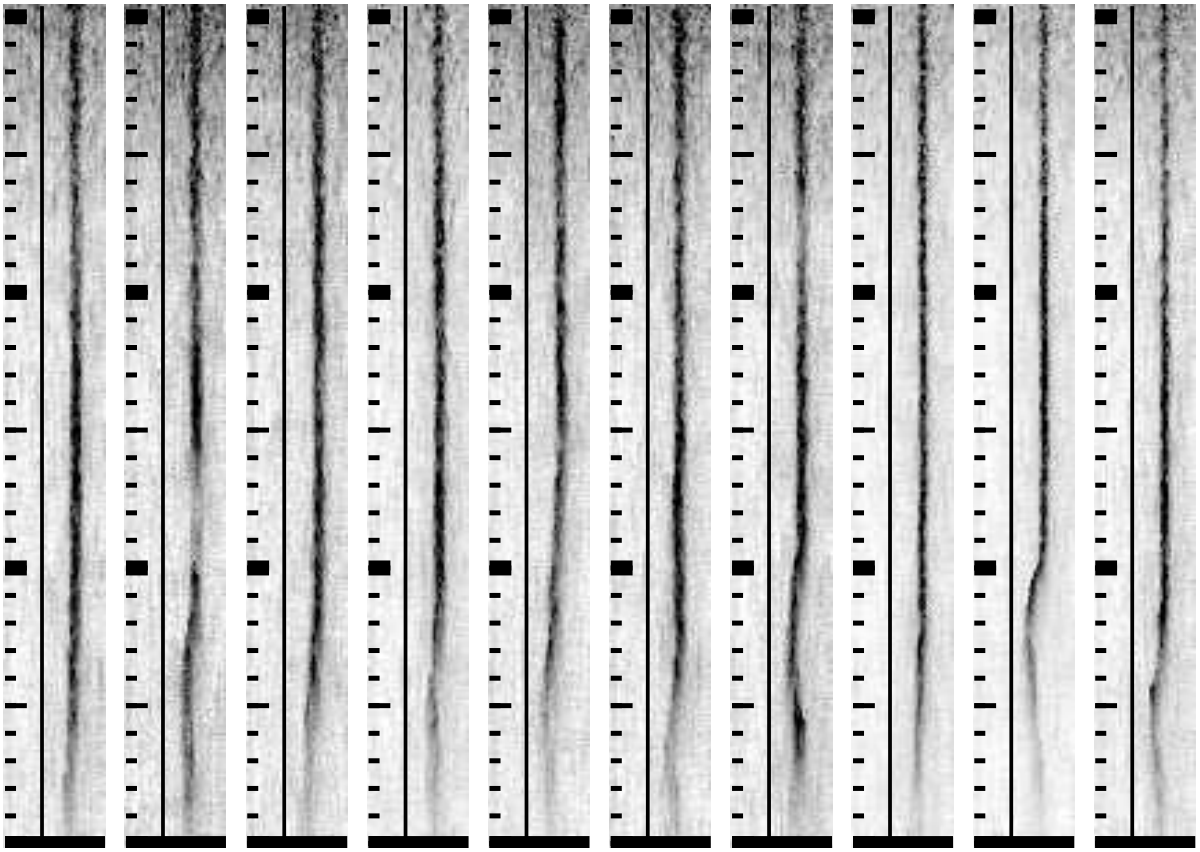

Figure 9. KTV in a 99% N_2 / 1% Kr Mach 2.75 turbulent boundary layer with a Re_Θ=800. Flow is left to right. Inverted intensity scale. The write location is marked by a vertical, thin black line. The camera gate is fixed to include only the read laser pulses. The delay between the write and read lines is 2 µs. Major tick marks at 10 mm intervals.

For each case, Re_Θ = 800, 1400, 2400, agreement between the three mean velocity profiles (KTV, Pitot, and VT Applet) is good, particularly between the Pitot and KTV measurements. The small discrepancy between the VT applet and the measurements may be because it is assumed that there is no pressure history (flat plate) and the transition occurs at the nozzle throat with the VT Applet calculations. Boundary-layer trips were placed near the throat; however, particularly for the Re_Θ = 800 case, the Reynolds number may not be sufficient to result in an equilibrium turbulent boundary layer at the measurement location which was $\approx$ 500 mm from the throat. KTV results near the windtunnel wall ($y/\delta_{99} < 0.1$) are not reported because the Gaussian fits to the read data were found to be unreliable. The lack of repeatable results close to the windtunnel wall ($y/\delta_{99} < 0.1$) is likely due to the high levels of fluctuation which smear the KTV tracer, yielding low SNR from the read pulse. Further study is required to confirm this.

Uncertainty in the velocimetry data was estimated following Moffat.[58] For the Pitot-derived velocity data, we assume that the uncertainty is determined by the reservoir temperature, Pitot pressure, and static pressure as

$$\delta U_{\text{Pitot}} = \left[\left(\delta P_{02} \frac{\partial U}{\partial P_{02}} \right)^2 + \left(\delta P_\infty \frac{\partial U}{\partial P_\infty} \right)^2 + \left(\delta T_\infty \frac{\partial U}{\partial T_\infty} \right)^2 \right]^{\frac{1}{2}}. \tag{10}$$

The uncertainty in Pitot-derived velocity from the Pitot pressure and static pressure can be determined using the Rayleigh-Pitot Probe Formula (Eq. 4). The uncertainty in the pressure transducer response is from comparisons of in-house calibrations against high-accuracy Baratron pressure transducers. The uncertainty in Pitot-derived velocity from the reservoir temperature is determined using the sound speed and the measured unsteadiness during the test time (Fig. 8(a)).

For the KTV-derived velocity data, we assume that the uncertainty is determined by the uncertainty in the

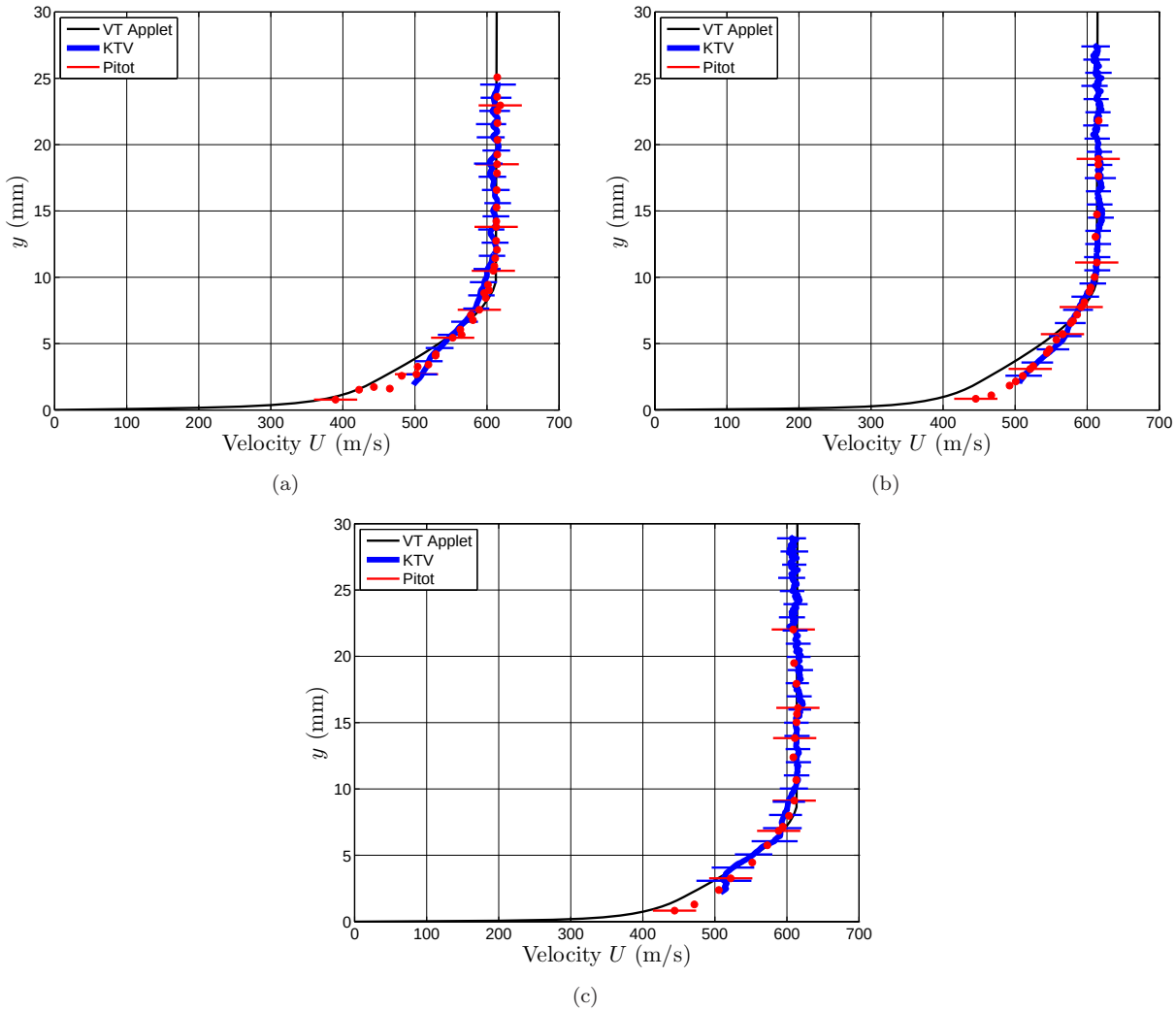

Figure 10. Profiles in a 99% N_2 / 1% Kr Mach 2.75 turbulent boundary layer with Re_Θ=800 (a), Re_Θ=1400 (b), and Re_Θ=2400 (c). Horizontal lines are error bars.

measured displacement distance of the metastable tracer and the timing accuracy of the experiment as

$$\delta U_{\mathrm{KTV}} = \left[\left(\delta \Delta x \frac{\partial U}{\partial \Delta x} \right)^2 + \left(\delta \Delta t \frac{\partial U}{\partial \Delta t} \right)^2 \right]^{\frac{1}{2}}. \tag{11}$$

The uncertainty in the measured displacement distance, Δx, of the metastable tracer is estimated as the 95% confidence bound on the write and read locations. The uncertainty Δt is estimated to be 50 ns, primarily due to fluorescence blurring as considered in Bathel et al.[59] From the manufacturers specification, we estimate that the jitter is relatively small, approximately 1 ns for each laser. The fluorescence blurring primarily occurs because of the time scale associated with the 819.0 nm $5p[3/2]_2 \rightarrow 5s[3/2]_1^o$ transition (25 ns);[60–63] so, we double this value and report that as the uncertainty in Δt.

VIII. Analysis

In this section, the velocity profiles in Fig. 10 are non-dimensionalized to analyze the KTV and Pitot data in the logarithmic and outer region of the boundary layer. The shear velocity, $u_\tau = \sqrt{\tau_w/\rho_w}$, is required and the method of calculation can be found from Eq. 17 in Appendix A.

The velocity data from the present study can be compared to the log law, $U^+ = 1/0.41\mathrm{Ln}(y^+)+5.2$, by using

the Van Driest I transformation, with $y^+ = \rho_w u_\tau u/\mu_w$ and $U^+ = U/u_\tau$. Following, Huang and Coleman[64] and Bradshaw,[65] the Van Driest transformed velocity can be written as

$$U^+_{VD} = \left[\sin^{-1}\left(\frac{R(U^+ + H)}{\sqrt{1+R^2H^2}}\right) - \sin^{-1}\left(\frac{RH}{\sqrt{1+R^2H^2}}\right)\right]/R, \tag{12}$$

where $R = M_\tau\sqrt{(\gamma-1)\,\mathrm{Pr}_t\,/2}$, $H = B_q/((\gamma-1)M_\tau^2)$, $M_\tau = u_\tau/c_w$, and $B_q = q_w/(\rho_w c_p u_\tau T_w)$. We assume the turbulent Prandtl number is $\mathrm{Pr}_t = 0.87$, and, assuming the Reynolds analogy holds, the heat-flux number is $B_q = c_f\rho_e U_e(T_w - T_r)/(2\,\mathrm{Pr}_e\,\rho_w u_\tau T_w)$.[66] The transformed KTV- and Pitot-derived velocity profiles are presented in Fig. 11(a). Also, in Fig. 11(a), we plot $U^+_{VD} = y^+$ and $U^+_{VD} = 1/0.41\mathrm{Ln}(y^+) + 5.2$. The transformed velocity follows the law of the wall in the logarithmic region with good agreement.

Fernholtz and Finley[67–69] outline a velocity-defect law to scale the outer layer of the turbulent boundary layer. In their work, Fernholtz and Finley define an integral length scale

$$\Delta^* = \int_0^\infty \frac{U_e^* - \bar{U}^*}{u_\tau} dy \tag{13}$$

where U_e^* and $\bar{U}^*$ are the edge and local mean velocities defined by

$$U^* = \frac{U_e}{b}\sin^{-1}\frac{2b^2U/U_e - a}{\sqrt{a^2+4b^2}} \tag{14}$$

and a and b are defined as

$$a = \frac{T_e}{T_w}\left(1 + r\frac{\gamma-1}{2}M_e^2\right) - 1 \tag{15}$$

$$b^2 = \frac{T_e}{T_w}\left(r\frac{\gamma-1}{2}M_e^2\right). \tag{16}$$

The resulting non-dimensional profiles are presented as Fig. 11(b). The scaling collapses the profiles satisfactorily. Also in Fig. 11(b), we plot $(U_e^* - \bar{U}^*)/(u_\tau) = -M\mathrm{Ln}(y/\Delta^*) - N$, with $M = 4.7, N = 6.74$. Here, M is not the Mach number but a constant that is consistent with the nomenclature of Fernholtz and Finley, where they propose the $(U_e^* - \bar{U}^*)/(u_\tau) = -4.7\mathrm{Ln}(y/\Delta^*) - 6.74$ relation for a turbulent boundary layer with zero pressure gradient. The agreement between the transformed KTV and Pitot velocity and

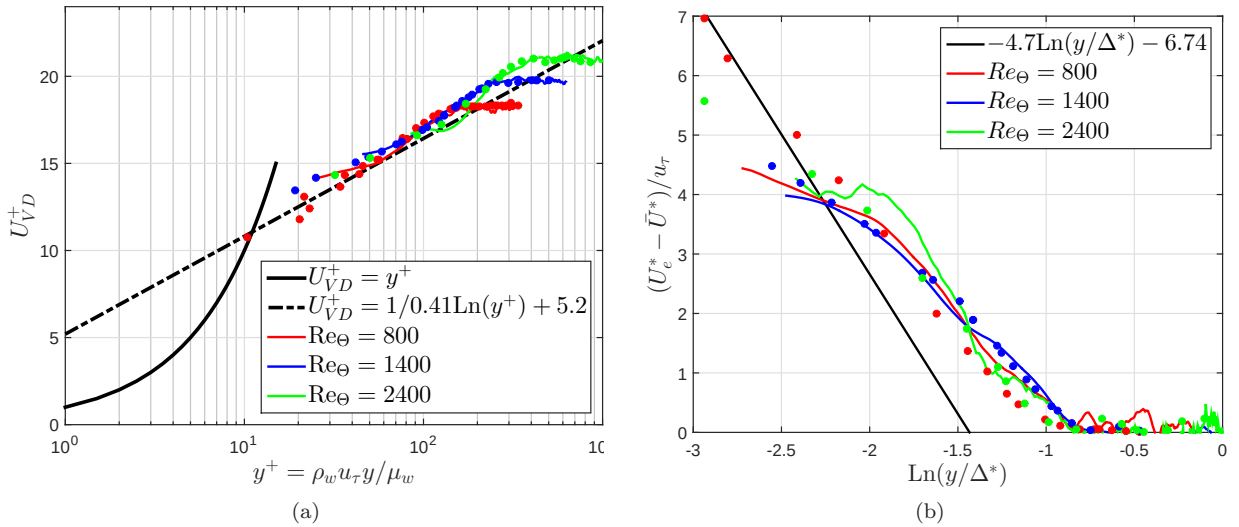

Figure 11. Non-dimensional velocimetry data for profiles in a 99% N_2 / 1% Kr Mach 2.75 turbulent boundary layer with Re_Θ=800,1400, 2400. Dots are Pitot-derived velocity. Lines are KTV-derived velocity. (a): Comparison of the Van Driest transformed velocity to the log law. (b): Velocity-defect law scaling of turbulent boundary layer.

$(U_e^* - \bar{U}^*)/(u_\tau) = -4.7\text{Ln}(y/\Delta^*) - 6.74$ is poor. Values of $\text{Ln}(y/\Delta^*) > -1.5$ at the boundary-layer edge ($(U_e^* - \bar{U}^*)/(u_\tau) = 0$), are consistent with data from the literature with a favorable pressure gradient.[67–69]

The RMS streamwise-velocity fluctuations, u'_{rms}, as measured by KTV and non-dimensionalized by the edge velocity are presented in Fig. 12(a). The KTV fluctuation measurements collapse for each case, except for the $Re_\Theta = 800$ case outside of the boundary layer. The reason for this raised level of fluctuation outside the boundary layer is unknown at the time of this writing.

The Morkovin[70] scaling ($\sqrt{\rho}u'_{rms}/\sqrt{\rho_w}u_\tau$) is applied to the data and presented in Fig. 12(b). In that figure, we overlay data from the literature from hot-wire anemometry (HWA) measurements from Klebanoff[71] recorded in a low-speed boundary layer (30 ft/s) and HWA and one- and two-component LDV measurements in a $M_e = 2.3$, $Re_\Theta = 4700$ boundary layer from Elena et al.[72] These data are also compared to DNS data in a $M_e = 2.3$, $Re_\Theta = 4450$ boundary layer from Martin.[73] The agreement between the KTV data from this work and the experimental and computational data is good for wall-normal distances $y/\delta_{99} > 0.2$.

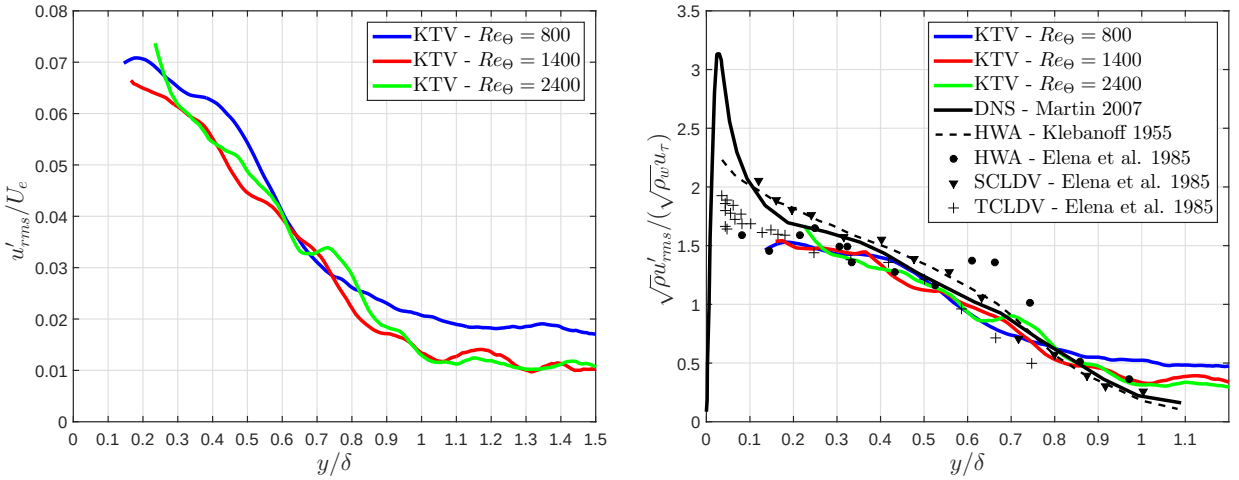

Figure 12. Streamwise-velocity fluctuation KTV data non-dimensionalized by the edge velocity in (a) and the Morkovin scaling in (b). The Morkovin scaled data are compared to historical data from Klebanoff[71] from an low-speed tunnel, Elena et al.[72] from a $M_e = 2.3$, $Re_\Theta = 4700$ boundary layer by hot-wire anemometry (HWA) and one- and two-component laser-Doppler velocimetry (LVD). These data are compared to direct numerical simulation (DNS) from Martin[73] from a $M_e = 2.3$, $Re_\Theta = 4450$ boundary layer.

IX. Conclusions and Future Work

To assess the potential use of the KTV technique to AEDC Hypervelocity Tunnel 9, the Mach 3 AEDC Calibration Tunnel was modified so that the unit Reynolds number could be prescribed at several values consistent with AEDC Tunnel 9 run conditions. The modification was comprised of an orifice plate, PVC pipe, and three perforated screens. These components were used to isothermally reduce the reservoir pressure, and thus the freestream unit Reynolds number.

In this work, we highlight the KTV measurement of a Mach 2.75 turbulent boundary layer at momentum thickness Reynolds numbers of $\text{Re}_\Theta = 800$, 1400, and 2400. Pitot-derived velocity data was also taken for the flowfield, and agreement between the KTV- and Pitot-derived velocity profiles is excellent. Moreover, the experimental profiles of velocity (both KTV and Pitot) agree with the predicted profiles from the Virginia Tech (VT) Compressible Turbulent Boundary Layer applet from Devenport and Schetz.[56,57]

The KTV- and Pitot-derived profiles of velocity are compared to the law of the wall with the application of the Van Driest I transformation, and agreement in the logarithmic region is good. From this, we conclude that KTV may be used to measure profiles of velocity in the logarithmic region of turbulent boundary layers.

The data is also scaled according to the velocity-defect law outlined in Fernholtz and Finley,[67–69] and the KTV and Pitot profiles collapse for the data taken at Re_Θ=800, 1400 and 2400. The KTV and Pitot data

do not follow the scaling reported by Fernholtz and Finley of $(U_e^* - \bar{U}^*)/(u_\tau) = -4.7\log(y/\Delta^*) - 6.74$. Near the abscissa of Fig. 11(b), in the wake region, the present data fall $\mathrm{Ln}(y/\Delta^+) > 1.5$. Fernholtz and Finely propose their parameters for the Reynolds number range $1500 < Re_{\delta 2} < 40000$ with zero pressure gradient. Here, $Re_{\delta 2} = \rho_e U_e \Theta/\mu_w$, and in this work, Re_Θ=800, 1400 and 2400 corresponds to $Re_{\delta 2}$= 350, 625, and 1100, respectively. Fernholtz and Finley assert that the agreement with the values $M = 4.7$ and $N = 6.74$ improves with increasing Reynolds number. The deviation from the scaling of the data from the present work in the outer region from the proposed form may be due to the low Reynolds number; however, the favorable pressure gradient history from the nozzle expansion in the present work may also play a role. For example, the data of Lewis et al.[74] characterize a compressible turbulent boundary layer with favorable and adverse pressure gradients. The Lewis et al. data from a favorable pressure gradient case is recast in Fernholtz and Finley[68] as Fig. 5.2.2. The Lewis et al. data show an offset to the right of $\mathrm{Ln}(y/\Delta^+) \approx 1.5$ near the abscissa (in the wake region) that is similar to the offset of the data presented in this work. Juxtaposed to this is the offset to the left of $\mathrm{Ln}(y/\Delta^+) \approx 1.5$ near the abscissa for an adverse pressure gradient in Fig. 5.3.5 of Fernholtz and Finley.[68] That is, the data in the present work is consistent with data from the literature for a favorable pressure gradient. From this, we conclude that KTV may be used to assess some fundamental characteristics of compressible turbulent boundary layers, such as pressure gradient history.

The KTV technique is used to quantify the streamwise-velocity fluctuations. The KTV fluctuation measurements collapse for each case, except for the $Re_\Theta = 800$ case outside of the boundary layer. The reason for this raised level of fluctuation outside the boundary layer is unknown at the time of this writing. The Morkovin scaling is applied to the RMS fluctuation data. The agreement between the computational and experimental data from the literature and KTV measurements from this work is good for wall-normal distances $y/\delta_{99} > 0.2$. Measurements below $y/\delta_{99} \approx 0.1 - 0.2$ are difficult to perform, and the issue in doing so with KTV may be that the tracer is smeared out because of the increase in velocity fluctuations near the wall (Fig. 12(b)). In the future, it may be possible to resolve the near-wall fluctuations by reducing the time between the write and read laser pulses so as to reduce the turbulent diffusion of the metastable Kr tracer.

Appendix A - Calculation of Skin Friction and Shear Velocity

To determine the shear velocity, $u_\tau = \sqrt{\tau_w/\rho_w}$, the shear stress at the wall, τ_w, must be determined. Following Xu and Martin,[75] the skin friction coefficient, $c_f = \tau_w/(0.5\rho_e U_e^2)$, can be determined from the Kármán[76]-Schoenherr[77] equation under the Van Driest II transformation as

$$\frac{1}{c_f F_c} = 17.08\left(\log_{10}(F_\Theta Re_\Theta)\right)^2 + 25.11\log_{10}(F_\Theta Re_\Theta) + 6.012 \tag{17}$$

where

$$F_c = 0.2rM_e^2/(\sin^{-1}(\alpha) + \sin^{-1}(\beta))^2 \tag{18}$$

$$F_\Theta = \mu_e/\mu_w, \tag{19}$$

and $r = 0.9$ is the recovery factor. The parameters α and β are computed as

$$\alpha = (2A^2 - B)/\sqrt{4A^2 + B^2} \tag{20}$$

$$\beta = B/\sqrt{4A^2 + B^2} \tag{21}$$

with

$$A^2 = 0.2rM_e^2/(T_w/T_e) \tag{22}$$

$$B = (1 + 0.2rM_e^2 - T_w/T_e)/(T_w/T_e). \tag{23}$$

Acknowledgments

The Air Force SFFP supported Zahradka and Parziale with a stipend for this work. The facilities and equipment were supplied by the Arnold Engineering Development Center (AEDC). We would like to acknowledge the encouragement of John Laffery and Dan Marren of AEDC White Oak. The authors would like to thank Mr. Brooks for his technical help with the Pitot-tube measurements. We would also like to acknowledge Joseph Wehrmeyer at Aerospace Testing Alliance (AEDC) for providing some of the laser systems.

References

[1]Bilardo, V. J., Curran, F. M., Hunt, J. L., Lovell, N. T., Maggio, G., Wilhite, A. W., and McKinney, L. E., "The Benefits of Hypersonic Airbreathing Launch Systems for Access to Space," *Proceedings of 39TH AIAA/ASME/SAE/ASEE Joint Propulsion Conference and Exhibit*, AIAA-2003-5265, Huntsville, Alabama, 2003. doi: 10.2514/6.2003-5265.

[2]Woolf, A. F., "Conventional Prompt Global Strike and Long-Range Ballistic Missiles: Background and Issues," R41464, 2014, Congressional Research Service.

[3]Candler, G. V., "Rate-dependent energetic processes in hypersonic flows," *Progress in Aerospace Sciences*, Vol. 72, 2015, pp. 37–48. doi: 10.1016/j.paerosci.2014.09.006.

[4]Schwartzentruber, T. E. and Boyd, I. D., "Progress and future prospects for particle-based simulation of hypersonic flow," *Progress in Aerospace Sciences*, Vol. 72, 2015, pp. 66–79. doi: 10.1016/j.paerosci.2014.09.003.

[5]Bose, D., Brown, J. L., Prabhu, D. K., Gnoffo, P., Johnston, C. O., and Hollis, B., "Uncertainty Assessment of Hypersonic Aerothermodynamics Prediction Capability," *Journal of Spacecraft and Rockets*, Vol. 50, No. 1, 2013, pp. 12–18. doi: 10.2514/1.A32268.

[6]Marren, D., Lewis, M., and Maurice, L. Q., "Experimentation, Test, and Evaluation Requirements for Future Airbreathing Hypersonic Systems," *Journal of Propulsion and Power*, Vol. 17, No. 6, 2001, pp. 1361–1365. doi: 10.2514/2.5888.

[7]McKeon, B., Comte-Bellot, G., Foss, J., Westerweel, J., Scarano, F., Tropea, C., Meyers, J., Lee, J., Cavone, A., Schodl, R., Koochesfahani, M., Andreopoulos, Y., Dahm, W., Mullin, J., Wallace, J., Vukoslavevi, P., Morris, S., Pardyjak, E., and Cuerva, A., "Velocity, Vorticity, and Mach Number," *Springer Handbook of Experimental Fluid Mechanics*, edited by Tropea, C. and Yarin, A. L. and Foss, J. F., Springer, 2007, pp. 215–471.

[8]Koochesfahani, M. M. and Nocera, D. G., "Molecular Tagging Velocimetry," *Springer Handbook of Experimental Fluid Mechanics*, edited by Tropea, C. and Yarin, A. L. and Foss, J. F., Springer, 2007.

[9]Haertig, J., Havermann, M., Rey, C., and George, A., "Particle Image Velocimetry in Mach 3.5 and 4.5 Shock-Tunnel Flows," *AIAA Journal*, Vol. 40, No. 6, 2002, pp. 1056–1060. doi: 10.2514/2.1787.

[10]Loth, E., "Compressibility and Rarefaction Effects on Drag of a Spherical Particle," *AIAA Journal*, Vol. 46, No. 9, 2008, pp. 2219–2228. doi: 10.2514/1.28943.

[11]Hsu, A. G., Srinivasan, R., Bowersox, R. D. W., and North, S. W., "Molecular Tagging Using Vibrationally Excited Nitric Oxide in an Underexpanded Jet Flowfield," *AIAA Journal*, Vol. 47, No. 11, 2009, pp. 2597–2604. doi: 10.2514/1.39998.

[12]Hsu, A. G., Srinivasan, R., Bowersox, R. D. W., and North, S. W., "Two-component molecular tagging velocimetry utilizing NO fluorescence lifetime and NO_2 photodissociation techniques in an underexpanded jet flowfield," *Applied Optics*, Vol. 48, No. 22, 2009, pp. 4414–4423. doi: 10.1364/AO.48.004414.

[13]Sánchez-González, R., Srinivasan, R., Bowersox, R. D. W., and North, S. W., "Simultaneous velocity and temperature measurements in gaseous flow fields using the VENOM technique," *Optics Letters*, Vol. 36, No. 2, 2011, pp. 196–198. doi: 10.1364/OL.36.000196.

[14]Sánchez-González, R., Bowersox, R. D. W., and North, S. W., "Simultaneous velocity and temperature measurements in gaseous flowfields using the vibrationally excited nitric oxide monitoring technique: a comprehensive study," *Applied Optics*, Vol. 51, No. 9, 2012, pp. 1216–1228. doi: 10.1364/AO.51.001216.

[15]Sánchez-González, R., Bowersox, R. D. W., and North, S. W., "Vibrationally excited NO tagging by NO($A^2\Sigma^+$) fluorescence and quenching for simultaneous velocimetry and thermometry in gaseous flows," *Optics Letters*, Vol. 39, No. 9, 2014, pp. 2771–2774. doi: 10.1364/OL.39.002771.

[16]Dam, N., Klein-Douwel, R. J. H., Sijtsema, N. M., and ter Meulen, J. J., "Nitric oxide flow tagging in unseeded air," *Optics Letters*, Vol. 26, No. 1, 2001, pp. 36–38. doi: 10.1364/OL.26.000036.

[17]Sijtsema, N. M., Dam, N. J., Klein-Douwel, R. J. H., and ter Meulen, J. J., "Air Photolysis and Recombination Tracking: A New Molecular Tagging Velocimetry Scheme," *AIAA Journal*, Vol. 40, No. 6, 2002, pp. 1061–1064. doi: 10.2514/2.1788.

[18]Van der Laan, W. P. N., Tolboom, R. A. L., Dam, N. J., and ter Meulen, J. J., "Molecular tagging velocimetry in the wake of an object in supersonic flow," *Experiments in Fluids*, Vol. 34, No. 4, 2003, pp. 531–534. doi: 10.1007/s00348-003-0593-1.

[19]Miles, R., Cohen, C., Connors, J., Howard, P., Huang, S., Markovitz, E., and Russell, G., "Velocity measurements by vibrational tagging and fluorescent probing of oxygen," *Optics Letters*, Vol. 12, No. 11, 1987, pp. 861–863. doi: 10.1364/OL.12.000861.

[20]Miles, R., Connors, J., Markovitz, E., Howard, P., and Roth, G., "Instantaneous profiles and turbulence statistics of supersonic free shear layers by Raman excitation plus laser-induced electronic fluorescence (RELIEF) velocity tagging of oxygen," *Experiments in Fluids*, Vol. 8, No. 1-2, 1989, pp. 17–24. doi: 10.1007/BF00203060.

[21]Miles, R. B., Zhou, D., Zhang, B., and Lempert, W. R., "Fundamental Turbulence Measurements by RELIEF Flow Tagging," *AIAA Journal*, Vol. 31, No. 3, 1993, pp. 447–452. doi: 10.2514/3.11350.

[22]Miles, R. B. and Lempert, W. R., "Quantitative Flow Visualization in Unseeded Flows," *Annual Review of Fluid Mechanics*, Vol. 29, No. 1, 1997, pp. 285–326. doi: 10.1146/annurev.fluid.29.1.285.

[23]Miles, R. B., Grinstead, J., Kohl, R. H., and Diskin, G., "The RELIEF flow tagging technique and its application in engine testing facilities and for helium-air mixing studies," *Measurement Science and Technology*, Vol. 11, No. 9, 2000, pp. 1272–1281. doi: 10.1088/0957-0233/11/9/304.

[24]Michael, J. B., Edwards, M. R., Dogariu, A., and Miles, R. B., "Femtosecond laser electronic excitation tagging for quantitative velocity imaging in air," *Applied Optics*, Vol. 50, No. 26, 2011, pp. 5158–5162. doi: 10.1364/AO.50.005158.

[25]Edwards, M. R., Dogariu, A., and Miles, R. B., "Simultaneous Temperature and Velocity Measurements in Air with Femtosecond Laser Tagging," *AIAA Journal*, Vol. 53, No. 8, 2015, pp. 2280–2288. doi: 10.2514/1.J053685.

[26]McDaniel, J. C., Hiller, B., and Hanson, R. K., "Simultaneous multiple-point velocity measurements using laser-induced iodine fluorescence," *Optics Letters*, Vol. 8, No. 1, 1983, pp. 51–53. doi: 10.1364/OL.8.000051.

[27]Balla, R. J., "Iodine Tagging Velocimetry in a Mach 10 Wake," *AIAA Journal*, Vol. 51, No. 7, 2013, pp. 1–3. doi: 10.2514/1.J052416.

[28]Lempert, W. R., Jiang, N., Sethuram, S., and Samimy, M., "Molecular Tagging Velocimetry Measurements in Supersonic Microjets," *AIAA Journal*, Vol. 40, No. 6, 2002, pp. 1065–1070. doi: 10.2514/2.1789.

[29]Lempert, W. R., Boehm, M., Jiang, N., Gimelshein, S., and Levin, D., "Comparison of molecular tagging velocimetry data and direct simulation Monte Carlo simulations in supersonic micro jet flows," *Experiments in Fluids*, Vol. 34, No. 3, 2003, pp. 403–411. doi: 10.1007/s00348-002-0576-7.

[30]Handa, T., Mii, K., Sakurai, T., Imamura, K., Mizuta, S., and Ando, Y., "Study on supersonic rectangular microjets using molecular tagging velocimetry," *Experiments in Fluids*, Vol. 55, No. 5, 2014, pp. 1–9. doi: 10.1007/s00348-014-1725-5.

[31]Boedeker, L. R., "Velocity measurement by H_2O photolysis and laser-induced fluorescence of OH," *Optics Letters*, Vol. 14, No. 10, 1989, pp. 473–475. doi: 10.1364/OL.14.000473.

[32]Wehrmeyer, J. A., Ribarov, L. A., Oguss, D. A., and Pitz, R. W., "Flame Flow Tagging Velocimetry with 193-nm H_2O Photodissociation," *Applied Optics*, Vol. 38, No. 33, 1999, pp. 6912–6917. doi: 10.1364/AO.38.006912.

[33]Pitz, R. W., Lahr, M. D., Douglas, Z. W., Wehrmeyer, J. A., Hu, S., Carter, C. D., Hsu, K.-Y., Lum, C., and Koochesfahani, M. M., "Hydroxyl tagging velocimetry in a supersonic flow over a cavity," *Applied Optics*, Vol. 44, No. 31, 2005, pp. 6692–6700. doi: 10.1364/AO.44.006692.

[34]Hiller, B., Booman, R. A., Hassa, C., and Hanson, R. K., "Velocity visualization in gas flows using laser-induced phosphorescence of biacetyl," *Review of Scientific Instruments*, Vol. 55, No. 12, 1984, pp. 1964–1967. doi: 10.1063/1.1137687.

[35]Gendrich, C. P. and Koochesfahani, M. M., "A spatial correlation technique for estimating velocity fields using molecular tagging velocimetry (MTV)," *Experiments in Fluids*, Vol. 22, No. 1, 1996, pp. 67–77. doi: Springer.

[36]Gendrich, C. P., Koochesfahani, M. M., and Nocera, D. G., "Molecular tagging velocimetry and other novel applications of a new phosphorescent supramolecule," *Experiments in Fluids*, Vol. 23, No. 5, 1997, pp. 361–372. doi: 10.1007/s003480050123.

[37]Stier, B. and Koochesfahani, M. M., "Molecular tagging velocimetry (MTV) measurements in gas phase flows," *Experiments in Fluids*, Vol. 26, No. 4, 1999, pp. 297–304. doi: 10.1007/s003480050292.

[38]Parziale, N. J., Smith, M. S., and Marineau, E. C., "Krypton Tagging Velocimetry for Use in High-Speed Ground-Test Facilities," *Proceedings of AIAA SciTech 2015*, AIAA-2015-1484, Kissimmee, Florida, 2015. doi: 10.2514/6.2015-1484.

[39]Parziale, N. J., Smith, M. S., and Marineau, E. C., "Krypton tagging velocimetry of an underexpanded jet," *Applied Optics*, Vol. 54, No. 16, 2015, pp. 5094–5101. doi: 10.1364/AO.54.005094.

[40]Mills, J. L., Sukenik, C. I., and Balla, R. J., "Hypersonic Wake Diagnostics Using Laser Induced Fluorescence Techniques," *Proceedings of 42nd AIAA Plasmadynamics and Lasers Conference*, AIAA 2011-3459, Honolulu, Hawaii, 2011. doi: 10.2514/6.2011-3459.

[41]Balla, R. J. and Everhart, J. L., "Rayleigh Scattering Density Measurements, Cluster Theory, and Nucleation Calculations at Mach 10," *AIAA Journal*, Vol. 50, No. 3, 2012, pp. 698–707. doi: 10.2514/1.J051334.

[42]Lafferty, J. F. and Marren, D. E., "Hypervelocity Wind Tunnel No. 9 Mach 7 Thermal Structural Facility Verification and Calibration," NSWCDD/TR-95/231, 1996.

[43]Marren, D. and Lafferty, J., "The AEDC Hypervelocity Wind Tunnel 9," *Advanced Hypersonic Test Facilities*, American Institute of Aeronautics and Astronautics, 2002, pp. 467–478. doi: 10.2514/5.9781600866678.0467.0478.

[44]Eckbreth, A. C., *Laser Diagnostics for Combustion Temperature and Species*, Gordon and Breach Publications, 2nd ed., 1996.

[45]White, F., *Fluid Mechanics*, McGraw-Hill Education, 2015.

[46]Liepmann, H. W. and Roshko, A., *Elements of Gasdynamics*, John Wiley and Sons, Inc., 1957.

[47]Tracy, C. J. and Oskam, H., "Properties of metastable krypton atoms in afterglows produced in krypton and krypton–nitrogen mixtures," *The Journal of Chemical Physics*, Vol. 65, No. 5, 1976, pp. 1666–1671. doi: 10.1063/1.433312.

[48]Velazco, J. E., Kolts, J. H., and Setser, D. W., "Rate constants and quenching mechanisms for the metastable states of argon, krypton, and xenon," *The Journal of Chemical Physics*, Vol. 69, No. 10, 1978, pp. 4357–4373. doi: 10.1063/1.436447.

[49]Sobczynski, R. and Setser, D. W., "Improvements in the generation and detection of $Kr(^3P_0)$ and $Kr(^3P_2)$ atoms in a flow reactor: Decay constants in He buffer and total quenching rate constants for Xe, N_2, CO, H_2, CF_4, and CH_4," *The Journal of Chemical Physics*, Vol. 95, No. 5, 1991, pp. 3310–3324. doi: 10.1063/1.460837.

[50]Zayarnyi, D. A., Yu L'dov, A., and Kholin, I. V., "Deactivation of krypton atoms in the metastable $5s(^3P_2)$ state in collisions with krypton and argon atoms," *Quantum Electronics*, Vol. 39, No. 9, 2009, pp. 821. doi: 10.1070/QE2009v039n09ABEH013999.

[51]Hornung, H. G., "Experimental Hypervelocity Flow Simulation, Needs, Achievements and Limitations," *Proceedings of the First Pacific International Conference on Aerospace Science and Technology*, Taiwan, 1993.

[52]Marineau, E. C., Moraru, G. C., Lewis, D. R., Norris, J. D., Lafferty, J. D., and Johnson, H. B., "Investigation of Mach 10 Boundary Layer Stability of Sharp Cones at Angle-of-Attack, Part 1: Experiments," *Proceedings of AIAA SciTech 2015*, AIAA-2015-1737, Kissimmee, Florida, 2015. doi: 10.2514/6.2015-1737.

[53]Brooks, J., Gupta, A., Smith, M. S., and Marineau, E. C., "Development of Non-Intrusive Velocity Measurement Capabilities at AEDC Tunnel 9," *Proceedings of 52nd Aerospace Sciences Meeting, SciTech*, AIAA-2014-1239, National Harbor, Maryland, 2014. doi: 10.2514/6.2014-1239.

[54]Brooks, J. M., Gupta, A. K., Smith, M. S., and Marineau, E. C., "Development of Particle Image Velocimetry in a Mach 2.7 Wind Tunnel at AEDC White Oak," *Proceedings of 53nd Aerospace Sciences Meeting, SciTech*, AIAA-2015-1915, Kissimmee, Florida, 2015. doi: 10.2514/6.2015-1915.

[55]Walz, A., "Compressible Turbulent Boundary Layers With Heat Transfer and Pressure Gradient in Flow Direction," *Journal of Research of the National Bureau of Standards-B*, Vol. 63B, No. 1, 1959, pp. 53–70. doi: 10.6028/jres.063B.008.

[56]Devenport, W. J. and Schetz, J. A., "Boundary Layer Codes for Students in Java," *Proceedings of the ASME Fluids Engineering Division Summer Meeting*, No. FEDSM98-5139, ASME, Washington, DC, 1998.

[57]Devenport, W. J. and Schetz, J. A., "Heat Transfer Codes for Students in Java," *Proceedings of the 5th ASME/JSME Thermal Engineering Joint Conference*, No. AJTE99-6229, ASME, San Diego, California, 1999.

[58]Moffat, R. J., "Contributions to the Theory of Single-Sample Uncertainty Analysis," *Journal of Fluids Engineering*, Vol. 104, No. 2, 1982, pp. 250–258. doi: 10.1115/1.3241818.

[59]Bathel, B. F., Danehy, P. M., Inman, J. A., Jones, S. B., Ivey, C. B., and Goyne, C. P., "Velocity Profile Measurements in Hypersonic Flows Using Sequentially Imaged Fluorescence-Based Molecular Tagging," *AIAA Journal*, Vol. 49, No. 9, 2011, pp. 1883–1896. doi: 10.2514/1.J050722.

[60]Fonseca, V. and Campos, J., "Absolute transition probabilities of some Kr I lines," *Physica B+C*, Vol. 97, No. 2, 1979, pp. 312–314. doi: 10.1016/0378-4363(79)90064-0.

[61]Chang, R. S. F., Horiguchi, H., and Setser, D. W., "Radiative lifetimes and twobody collisional deactivation rate constants in argon for $Kr(4p^55p)$ and $Kr(4p^55p)$ states," *The Journal of Chemical Physics*, Vol. 73, No. 2, 1980, pp. 778–790. doi: 10.1063/1.440185.

[62]Whitehead, C. A., Pournasr, H., Bruce, M. R., Cai, H., Kohel, J., Layne, W. B., and Keto, J. W., "Deactivation of two-photon excited $Xe(5p^56p,6p',7p)$ and $Kr(4p^55p)$ in xenon and krypton," *The Journal of Chemical Physics*, Vol. 102, No. 5, 1995, pp. 1965–1980. doi: 10.1063/1.468763.

[63]Dzierżga, K., Volz, U., Nave, G., and Griesmann, U., "Accurate transition rates for the 5p-5s transitions in Kr I," *Physical Review A*, Vol. 62, No. 2, 2000, pp. 022505. doi: 10.1103/PhysRevA.62.022505.

[64]Huang, P. G. and Coleman, G. N., "Van Driest Transformation and Compressible Wall-Bounded Flows," *AIAA Journal*, Vol. 32, No. 10, 1994, pp. 2110–2113. doi: 10.2514/3.12259.

[65]Bradshaw, P., "Compressible Turbulent Shear Layers," *Annual Review of Fluid Mechanics*, Vol. 9, No. 1, 1977, pp. 33–52. doi: 10.1146/annurev.fl.09.010177.000341.

[66]Schlichting, H., *Boundary-Layer Theory*, Springer, 2000.

[67]Fernholtz, H. H. and Finley, P. J., "A Critical Compilation of Compressible Turbulent Boundary Layer Data," AGARD-223, 1977.

[68]Fernholtz, H. H. and Finley, P. J., "A Critical Commentary on Mean Flow Data for Two-Dimensional Compressible Turbulent Boundary Layers," AGARD-253, 1980.

[69]Smits, A. J. and Dussauge, J. P., *Turbulent Shear Layers in Supersonic Flow*, Springer, 2nd ed., 2006.

[70]Morkovin, M. V., "Effects of compressibility on turbulent flows," *Mécanique de la Turbulence*, 1962, pp. 367–380, CNRS.

[71]Klebanoff, P. S., "Characteristics of Turbulence in a Boundary Layer with Zero Pressure Gradient," NACA TR-1247, 1955.

[72]Elena, M., Lacharme, J. P., and Gaviglio, J., "Comparison of hot-wire and laser Doppler anemometry methods in supersonic turbulent boundary layers," *Proceedings of 2nd International Symposium on Laser Anemometry*, Miami Beach, Florida, 1985, pp. 151–157.

[73]Martin, M. P., "Direct numerical simulation of hypersonic turbulent boundary layers. Part 1. Initialization and comparison with experiments," *Journal of Fluid Mechanics*, Vol. 570, 2007, pp. 347–364. doi: 10.1017/S0022112006003107.

[74]Lewis, J. E., Gran, R. L., and Kubota, T., "An experiment on the adiabatic compressible turbulent boundary layer in adverse and favourable pressure gradients," *Journal of Fluid Mechanics*, Vol. 51, No. 4, 1972, pp. 657–672. doi: 10.1017/S0022112072001296.

[75]Xu, S. and Martin, M. P., "Assessment of inflow boundary conditions for compressible turbulent boundary layers," *Physics of Fluids*, Vol. 16, No. 7, 2004, pp. 2623–2639. doi: 10.1063/1.1758218.

[76]von Kármán, T., "Turbulence and Skin Friction," *Journal of the Aeronautical Sciences*, Vol. 1, No. 1, 1934, pp. 1–20. doi: 10.2514/8.5.

[77]Schoenherr, K. E., *Resistance of Flat Surfaces Moving Through a Fluid*, Vol. 40, 1932.